RIT WEBINARS

LEARN & INTERACT WITH RIT PRODUCT EXPERTS

ANYWHERE, ANYTIME

RIT™

Be the first to know about FREE monthly webinars from RIT!

CLICK TO SUBSCRIBE

RECEIVE EMAIL INVITATIONS FOR RIT WEBINARS

Discuss RIT product features with a high-level of interaction, lead by a medical physicist. A Q&A section follows each RIT webinar.

Conveniently choose between multiple time sessions for each RIT webinar, making viewing easy all around the world.

Never miss a webinar: All past webinars are posted on RIT's website so in-support customers can view them on demand.

RADIMAGE.COM

719-590-1077 • sales@radimage.com

Connect with RIT
@RIT4QA

Talbot-Lau X-ray phase contrast for tiling-based acquisitions without reference scanning

Sebastian Kaeppler[a)]
Pattern Recognition Lab, Friedrich-Alexander-University Erlangen-Nuremberg, Martensstr. 3, 91058 Erlangen, Germany

Maria Seifert, Florian Horn, Georg Pelzer, Jens Rieger, and Thilo Michel
Erlangen Centre for Astroparticle Physics, Friedrich-Alexander-University Erlangen-Nuremberg, Erwin-Rommel-Str. 1, 91058 Erlangen Germany

Andreas Maier
Pattern Recognition Lab, Friedrich-Alexander-University Erlangen-Nuremberg, Martensstr. 3, 91058 Erlangen, Germany

Gisela Anton
Erlangen Centre for Astroparticle Physics, Friedrich-Alexander-University Erlangen-Nuremberg, Erwin-Rommel-Str. 1, 91058 Erlangen Germany

Christian Riess
Pattern Recognition Lab, Friedrich-Alexander-University Erlangen-Nuremberg, Martensstr. 3, 91058 Erlangen, Germany

(Received 9 June 2016; revised 9 February 2017; accepted for publication 28 February 2017; published 20 April 2017)

Purpose: Grating-based Talbot-Lau interferometers are a popular choice for phase-contrast X-ray acquisitions. Here, an air reference scan has to be acquired prior to an object scan. This particularly complicates acquisition of large objects: large objects are tiled into multiple scans due to the small field of view of current gratings. However, phase reference drifts occurring between these scans may require to repeatedly move the object in and out of the X-ray beam to update the reference information.
Methods: We developed an image processing technique that completely removes the need for phase reference scans in tiled acquisitions. We estimate the reference from object scans using a tailored iterated robust regression, using a novel efficient optimizer.
Results: Our evaluation indicates that the estimated reference is not only close to the acquired reference but also improves the final image quality. We hypothesize that this is because we mitigate errors that are introduced when actually acquiring the reference phase.
Conclusion: Phase-contrast imaging of larger objects may benefit from computational estimation of phase reference data due to reduced scanning complexity and improved image quality. © *2017 American Association of Physicists in Medicine* [https://doi.org/10.1002/mp.12200]

Key words: grating interferometer, phase-contrast, reference image, x-ray imaging

1. INTRODUCTION

X-ray phase contrast (XPC) measures the phase-shift of an object at X-ray energies.[1] Recently, XPC research gained considerable momentum after presentation of the Talbot interferometer[2,3] and shortly thereafter the Talbot-Lau interferometer.[4] It provides three images showing X-ray absorption, differential phase, and darkfield. The clinical potential of these signals has been extensively investigated in subsequent works, using the phase as a stand-alone signal (e.g., in Refs. 5–7), phase in combination with absorption,[8] or the darkfield signal (e.g., Refs. 9–12). Specifically, phase-contrast and dark-field X-ray imaging of breast specimens have demonstrated improved soft-tissue visualization compared to absorption X-ray alone[13,14] and considerable effort is being made to translate phase-contrast X-ray in clinical practice.[15–17] One issue for translation is low fringe visibility with broad spectrum medical X-ray tubes and high photon energies. This has been addressed by optimized setups[16,18] and by using a phase grating with a duty cycle different than 0.5.[19]

While specialized setups with a small-field of view are already used in clinical trials,[20] several technological challenges still need to be tackled to allow widespread use of Talbot-Lau imaging in mammography and general radiography. Due to the G0 grating, X-ray flux is reduced by a factor of about two (the exact number depends on the G0 duty cycle). This is an inherent limitation of the Talbot-Lau system and needs to be compensated for by using high-power X-ray tubes. Furthermore, the G2 grating used to sample the Talbot pattern also reduces flux. As the G2 is positioned downstream of the object, any G2 absorption reduces dose efficiency. Assuming a perfect grating with a duty cycle of 0.5, dose efficiency is also reduced by a factor of two. However, some of this loss may be compensated by the G2 grating acting as an antiscatter grid.[21] Despite the above-mentioned advances in system design, reasonable visibilities can only be expected for X-ray spectra up to 100–120 kVp[18,22] due to limitations in grating manufacturing. Another limitation is the need for phase stepping which complicates the image acquisition. This can be alleviated by using electromagnetic

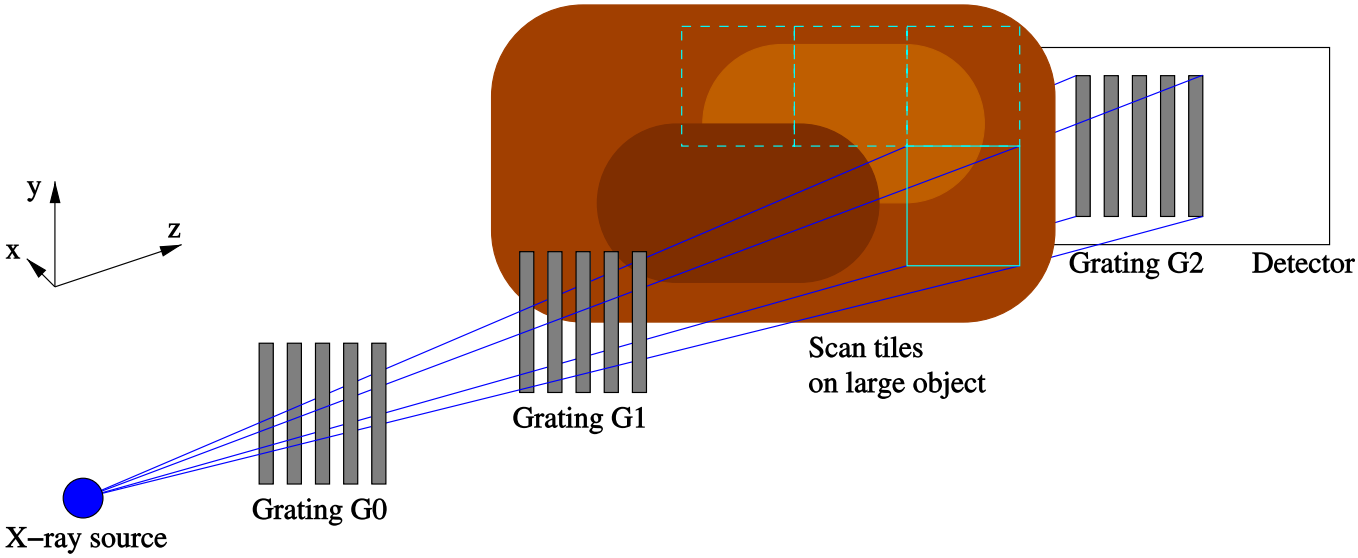

FIG. 1. Sketch of a Talbot-Lau interferometer scanning a large object. The interferometer consists of an X-ray source, three gratings, and an X-ray detector. Due to the limited field of view, objects larger than few centimeters must be captured in multiple acquisitions. One such acquisition is indicated by a solid frame. The interferometer has to be recalibrated between multiple acquisitions, requiring to move the object temporarily away from the field of view. In this work, we propose a computational method to avoid recalibration. [Color figure can be viewed at wileyonlinelibrary.com]

phase stepping,[23] by sacrificing image resolution with Moirè imaging[24] or a specially designed G2 grating,[21] or by a slit-scanning approach that sacrifices flux.[25] Unlike in absorption imaging, phase information can only be retrieved reliably up to a visibility-dependent noise level,[26] which may restrict the applicability of phase-contrast imaging for low-dose or CT applications. Moreover, obtaining quantitative CT measurements from polychromatic setups has to our knowledge only been shown for very clean laboratory data.[27] Despite these open problems, a slit-scanning interferometer was recently used to demonstrate high-energy large field-of-view (35 cm^2) dark-field lung imaging of living piglets.[22] While the scanning time of 40 s is still relatively high, the reported effective dose of less than 1 mSv is within clinical requirements.

Still, another serious challenge for the diagnostic applicability of Talbot-Lau interferometers lies in current manufacturing technology. The interferometer consists of three gratings G0, G1, and G2 with micrometer periods. It is currently not possible to build these gratings with a diameter larger than a few centimeters. While 1-D tiling of gratings has been reported recently,[28] first Talbot-Lau system will have to rely on creating a composite image.[29] The composite image can be generated by either naively stitching image tiles, or in the case of mammography by a smart slit-scanning mechanism.[22,25] Figure 1 shows an example sketch of a large object acquisition using multiple tiles.

In a single-image acquisition, setup disturbances are corrected by an additional so-called reference scan without an object in the beam path. The reference captures various influences like grating inhomogeneities and slight misalignments from calibration, mechanical motion, or temperature. A practical issue of obtaining a composite image lies in the fact that the calibration of the interferometer phase is not stable across multiple acquisitions, because effects from mechanical motion and temperature change over time. Thus, the reference has to be updated every few exposures. Updating the reference is highly impractical: the object or the X-ray device has to be moved mutiple times such that reference scans without the object in the beam path can be acquired. This is a laborious process that is furthermore prone to introduce additional image artifacts from object motion and new drift artifacts from to mechanical motion of the interferometer, thus defeating its purpose.

The drift problem is even amplified when moving away from a laboratory system towards clinical systems. Laboratory systems are typically mounted on vibration-dampening optical tables. When we modified our tiling-based setup to more closely mimic a clinical mammography system by mounting it vertically on a metal frame, we noticed that the phase drift increased. Observations of phase reference drift were first reported for micro CT imaging[7] and also recently for a slit-scanning interferometer mounted in a clinical mammography system.[25] During reference acquisition, radiation shielding must also ensure that X-rays scattered by the interferometer gratings do not reach the patient. These factors make the acquisition of reference scans highly undesirable in a clinical context.

In a previous work,[30] we demonstrated that tiling-based phase-contrast imaging using only one reference scan is possible. However, compared to using multiple reference images, this method suffers from ringing artifacts at strong object edges.

In this paper, we propose a method for estimating the reference phase directly from the data of the object scans, without acquiring any reference images. This makes it possible to perform composite phase-contrast scans in one sweep. To our knowledge, this is the first method that allows to completely omit the reference scan. It expedites the acquisition, intrinsically prevents realignment problems from interleaved reference scans and simplifies the overall scanning protocol.

Using images of breast mastectomy specimens, we demonstrate that the proposed method even improves the image quality, because it adapts to slight grating misalignments, which the acquired references cannot do.

The paper is organized as follows: we present the mathematical model and the computational algorithm in Section 2, with an overview in Section 1, and the individual components in the following subsections. Our experimental results are presented in Sections 3 and 4. We end with a short discussion in Section 5 and conclusion in Section 6.

2. METHODS

When performing Talbot-Lau interferometry for phase-contrast imaging, two differential phase images are required: the differential reference phase **R**, recorded without any object in the beam path, and the differential object phase **O** with the scanned object in the beam path. In practice, **R** and **O** are computational images, i.e., the phase information is reconstructed from a set of so-called phase step images. For clarity, we subsequently do not denote this intermediate reconstruction step. Thus, given **R** and **O**, the normalized differential phase-contrast image **P** is computed as the difference of the two scans:

$$\mathbf{P} = \mathbf{O} - \mathbf{R}. \tag{1}$$

In an ideal interferometer, the reference phase would be constant over the whole image and would only depend on the alignment of the G1 and G2 gratings perpendicular to the grating bars. In a real interferometer, several effects contribute to the reference phase. Grating inhomogeneities, by e.g., slightly varying grating height or period, or support structures on the gratings typically cause local variations of the reference phase. These variations are easily captured by the reference scan, as they only depend on the coarse alignment of the gratings on a scale of the pixel size. Stronger variations in the low-frequency reference phase are mostly due to the alignment and temperature of the gratings. Due to phase wrapping around 2π, these phase variations typically show up as Moirè effects in the measured phase images. Two example phase reference images, captured 50 min apart, are shown in Fig. 2.

The sensitivity of the reference phase with respect to alignment can be shown by considering the case of an in-plane movement m of the G2 grating perpendicular to the grating bars. Assuming perfect gratings, the change of the reference phase is given by $\frac{2\pi m}{p}$, with p being the period of the G2 grating. As p is typically in the range of a few micrometers, extreme stability of the interferometer is required to keep the reference phase stable. Besides changes of the reference phase that are constant over the image, setups with low stability oftentimes exhibit also phase ramps. An example phase ramp is shown in Fig. 2(c). These effects were first reported by Tapfer et al.[7] for a micro CT system. The authors linked the drifts to thermal expansion of the gratings and their holding mechanisms, as well as to changes in grating alignment. However, to our knowledge, there exist no study that directly links changes in grating temperature or position to the corresponding change in reference phase. Until now, the drift problem has been mitigated by frequently reacquiring the reference images. This approach becomes unpractical in a clinical scenario, where absolute stability of the interferometer cannot be guaranteed and where reacquisition of the reference phase may not always be possible.

2.A. Method overview

In a multiexposure acquisition (tiling-based or slit scanning), a set $\mathcal{O} = \{\mathbf{O}_1, \ldots, \mathbf{O}_N\}$ of N object images $\mathbf{O}_i$, $1 \leq i \leq N$ is obtained. We show that for sufficiently large N, *virtual* reference images $r(\mathcal{O}, i)$ can be computed as a function of the object scans, which allows to omit acquisition of all reference images. Consequently, multiexposure differential phase images $\mathbf{P}'_i$ can be computed as:

$$\mathbf{P}'_i = \mathbf{O}_i - r(\mathcal{O}, i). \tag{2}$$

The estimation of the virtual reference is composed of three processing steps, illustrated in Fig. 3. A phase

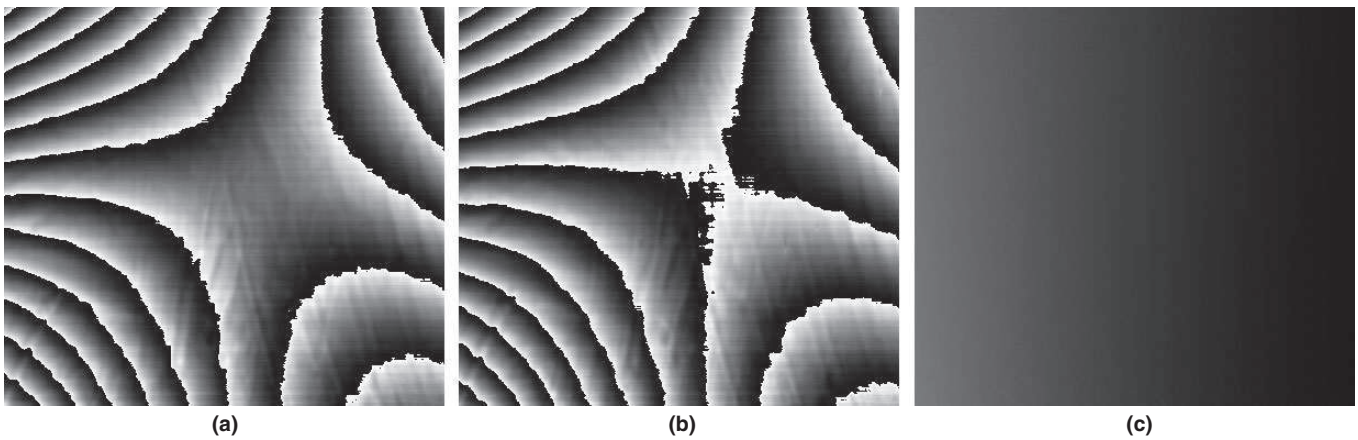

FIG. 2. Illustration of the reference phase drift. (a) Reference phase of first measurement. (b) Reference phase of second measurement, acquired approximately 50 min after the first measurement. (c) Difference between the unwrapped reference images. In this example, a constant and a linear drift in x-direction are dominant.

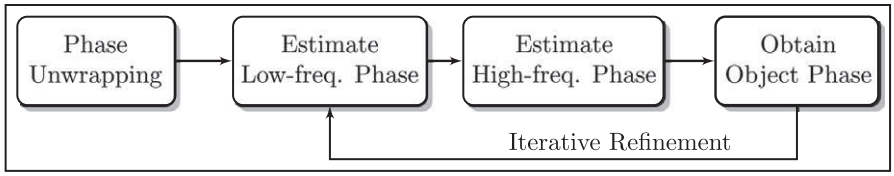

FIG. 3. Flowchart of the estimation of the virtual reference phase. After estimation of a first solution, the result is refined by iteratively excluding pixels with strong object signals.

unwrapping algorithm is applied to the measured object scan to remove phase discontinuities. Then, the virtual reference scans $r(\mathcal{O}, i)$ are estimated. This process is based upon a model of the reference phase that distinguishes a low-frequency and a high-frequency part of the signal. We first estimate the low-frequency part, then in a second step the high-frequency part. The resulting reference can be iteratively refined by omitting pixels that show strong object signals from the estimation.

2.B. Phase unwrapping

Prior to any other processing, phase unwrapping is applied to all object scans. Due to the measurement principle inherent to interferometric imaging, phase measurements are only known up to a multiple of 2π. Phase shifts outside of the range $[-\pi; \pi]$ are *phase wrapped*, i.e., the measured phase shift does not correspond to the real phase shift. One source of phase wraps in differential phase-contrast images are strong phase gradients e.g., at object/air borders. However, the most dominant cause of phase wraps is the Moirè patterns arising from slight grating misalignment. Phase wraps typically result in strong discontinuities in the measured image and thus hamper the separation of object and reference information. The problem of removing phase wraps, also called *phase unwrapping*, has been studied extensively in the field of synthetic aperture radio (SAR). Ideally, phase unwrapping algorithms estimate the true phase, up to a global (per image) constant. Exact computation of the true phase is an integer programming problem that is computationally hard. Thus, we utilize the seminal method of Constantini,[31] which reformulates the integer program as an efficiently solvable minimum-cost network flow. In pilot experiments, this method effectively removed all Moirè-induced phase wraps. The phase unwrapping method is applied to all object images $\mathbf{O}_i$. The images after unwrapping are referred to as $\mathbf{O}_i^{\mathrm{u}}$. An example unwrapping result is shown in Fig. 4.

2.C. Model of the reference phase

The unwrapped reference phase consists of a strong low-frequency component and a somewhat weaker high-frequency component. We separate a virtual reference image $r(\mathcal{O}, i)$ into its high-frequency component $\mathbf{R}_i^{\mathrm{hf}}$ and its low-frequency component $\mathbf{R}_i^{\mathrm{lf}}$,

$$r(\mathcal{O}, i) = \mathbf{R}_i^{\mathrm{lf}} + \mathbf{R}_i^{\mathrm{hf}}. \tag{3}$$

This separation into individual parts allows to tailor the estimation to the different root causes that dominate each part. In previous studies, the low-frequency component has been attributed to a drifting grating alignment that is caused by mechanical and thermal effects.[7] This is in line with our observation that the low-frequency phase signal arises from phase unwrapping of the Moirè pattern, which indeed depends on the grating alignment. Conversely, the residual high-frequency component exhibits a grating-like structure, which we mainly attribute to imperfections of the interferometer gratings. This is also in line with the additional observation that the low-frequency part slowly varies from scan

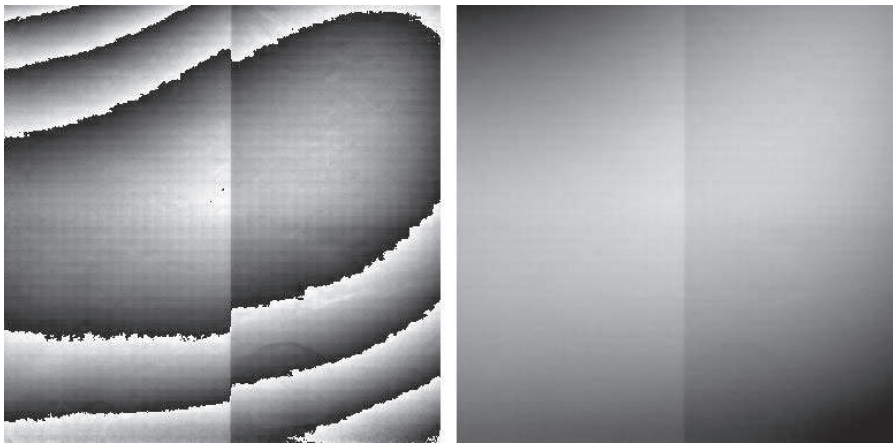

FIG. 4. Illustration of the phase unwrapping process for one tile of an image of a human breast mastectomy specimen: (a) Object scan $\mathbf{O}_i$. (b) The same image after unwrapping, $\mathbf{O}_i^{\mathrm{u}}$.

to scan, while the high-frequency part remains relatively constant.

We estimate $r(\mathcal{O}, i)$ from the unwrapped images in three steps, namely first $\mathbf{R}_i^{\mathrm{lf}}$, then $\mathbf{R}_i^{\mathrm{hf}}$, and finally we iteratively refine both estimates. These steps are described in the next Sections below.

2.D. Estimation of the low-frequency reference phase

The estimation of the low-frequency reference phase is based on robust regression. We assume that correlations in the low-frequency part of the object tile images can be attributed to the reference phase. This holds as long as the object information is different (and hence, uncorrelated) across multiple images, which typically is the case in a composite acquisition. Due to drifts, the low-frequency reference may slightly vary between images. Thus, we seek a low-frequency signal which is correlated over all images, but that may still change smoothly between consecutive images.

For each individual image, we model the shape of the low-frequency phase as a 2-D polynomial image of degree d. Let $\mathbf{p}_i$ denote the polynomial coefficients for image i, then $\mathbf{R}_i^{\mathrm{lf}}$ can be rewritten as

$$\mathbf{R}_i^{\mathrm{lf}} = \mathbf{M} \cdot \mathbf{p}_i. \tag{4}$$

Here, M denotes the mapping matrix of size $S \times d'$, where S is the number of image pixels and d' is the number of polynomial coefficients.

If the coefficients $\mathbf{p}_i$ are estimated from each image individually, as stated in Eq. 4, strong object signals particularly at object boundaries can bias the fit. As indicated above, low-frequency drifts, e.g., due to thermal effects, can be expected to change the reference phase only gradually. This is modeled by an additional constraint on the variation between consecutive images, which at the same time suppresses residual low-frequency object information. Thus, we estimate the total set of polynomial coefficients, $\mathbf{P} = [\mathbf{p}_1, \mathbf{p}_2, \ldots \mathbf{p}_N]$, as

$$\arg\min_{\mathbf{P}} \sum_{i=1}^{N} \|\mathbf{M} \cdot \mathbf{p}_i - \mathbf{O}_i^{\mathrm{u}}\|_1 + \sum_{i=1}^{N-1} \frac{1}{2} \|\mathbf{p}_i - \mathbf{p}_{i+1}\|_{\mathbf{w}}^2. \tag{5}$$

The optimization problem in Eq. 5 consists of two parts. The first part seeks to minimize the discrepancy between the low-frequency reference phase and the object images, weighted by the L1-norm. Compared to the L2-norm, this strategy improves robustness with respect to strong object signals. The second part promotes smooth changes of the polynomial coefficients (and hence also $\mathbf{R}^{\mathrm{lf}}$) across consecutively acquired tiles. This is achieved by penalizing the weighted least squares distance between the coefficient vectors of consecutive images. Here, the weighting vector $\mathbf{w}$ models our observation that the lower degree components of the polynomials experience a stronger drift than the higher ones. The optimization of the resulting objective function is a mixed L1-/L2-weighted problem. The size of the combined measurements matrices makes direct optimization of Eq. 5 infeasible for typical image sizes (see Appendix A for details). An efficient solution to this type of problem has, to our knowledge, not yet been considered in optimization literature. However, we found an efficient solution to Eq. 5 by transforming it into an equivalent constrained problem that can be solved more easily by applying the Alternating Direction Method of Multipliers (ADMM,[32]),

$$\begin{aligned} &\arg\min_{\mathbf{P},\mathbf{Z}} \sum_{i=1}^{N} \|\mathbf{z}_i\|_1 + \sum_{i=1}^{N-1} \frac{1}{2} \|\mathbf{p}_i - \mathbf{p}_{i+1}\|_{\mathbf{w}}^2 \\ &\quad \text{subject to } \mathbf{z}_i = \mathbf{M} \cdot \mathbf{p}_i - \mathbf{O}_i^{\mathrm{u}} \quad \forall i. \end{aligned} \tag{6}$$

It can be shown that the ADMM applied to this problem corresponds to iteratively solving a soft-thresholding and a generalized Tikhonov-regularized least squares problem. We present a full derivation of the optimization method and additional details in Appendix A. Example estimates for the low-frequency reference phase are shown in Fig. 5.

FIG. 5. Estimation of the low-frequency phase for one tile of an image of a human breast mastectomy specimen: (a) Phase unwrapped object scan $\mathbf{O}_i^{\mathrm{u}}$. (b) Estimated low frequency reference phase $\mathbf{R}_i^{\mathrm{lf}}$. (c) Intermediate estimate of differential phase $\mathbf{P}_i^{\mathrm{hf}}$.

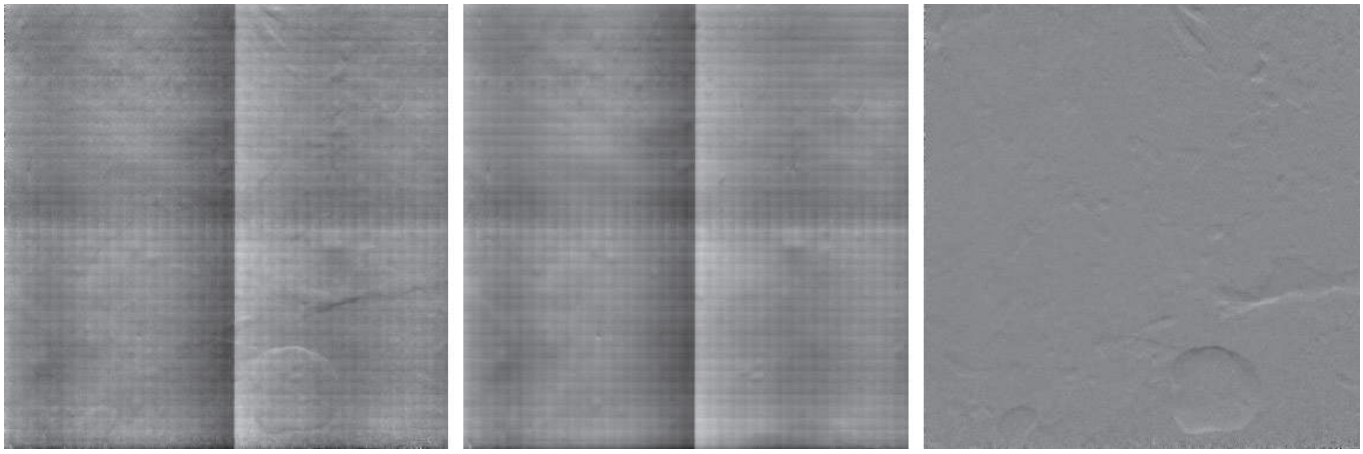

FIG. 6. Estimation of the high-frequency phase for one tile of an image of a human breast mastectomy specimen: (a) Intermediate estimate of differential phase $\mathbf{P}_i^{\mathrm{hf}}$. (b) Estimated high frequency reference phase $\mathbf{R}_i^{\mathrm{hf}}$. (c) Final differential phase image $\mathbf{P}'_i$. The grid-like reference signal is separated from the features of the specimen.

2.E. Estimation of the high-frequency reference phase

An intermediate estimate $\mathbf{P}_i^{\mathrm{hf}}$ of each differential phase image can be computed by subtracting the estimated low-frequency reference from $\mathbf{O}_i^{\mathrm{u}}$,

$$\mathbf{P}_i^{\mathrm{hf}} = \mathbf{O}_i^{\mathrm{u}} - \mathbf{R}_i^{\mathrm{lf}}. \tag{7}$$

The goal is to compute the high-frequency reference phase $\mathbf{R}_i^{\mathrm{hf}}$ from $\mathbf{P}_i^{\mathrm{hf}}$. The estimation makes use of the prior observations that the object signal varies between images, but the high-frequency reference $\mathbf{R}_i^{\mathrm{hf}}$ mostly consists of grating artifacts and remains relatively constant over consecutive acquisitions. In absence of any other model for $\mathbf{R}_i^{\mathrm{hf}}$, we perform a pixel-wise estimation of $\mathbf{R}_i^{\mathrm{hf}}$ over a range of $2a$ images as

$$\arg\min_{\mathbf{R}_i^{\mathrm{hf}}} \sum_{j=\max(i-a,1)}^{\min(i+a,N)} \|\mathbf{P}_j^{\mathrm{hf}} - \mathbf{R}_i^{\mathrm{hf}}\|_1. \tag{8}$$

Equation 8 states that subtracting the estimated reference scan for image i should minimize the L1-norms of all images over a window of size $2a$ around i. As with the estimation of the low-frequency part, the L1-norm is more robust and better rejects strong object signals than the L2-norm. Equation 9 is equivalent to estimating the pixel-wise median of the images in the respective windows.[33] Similar as with the low-frequency reference phase, the use of neighboring images allows the separation of the high-frequency reference from the object signal, even if they show spectral overlap, as long as the object signals in the window are not correlated.

After computing the high-frequency part of the virtual reference scan, the differential phase images can be computed as

$$\mathbf{P}'_i = \mathbf{P}_i^{\mathrm{hf}} - \mathbf{R}_i^{\mathrm{hf}}. \tag{9}$$

This step concludes the regular processing step of the algorithm. Example results for the high-frequency reference phase are shown in Fig. 6.

2.F. Refinement step

Optionally, the results can be iteratively refined by excluding individual pixels containing strong object signals from the estimation. To this end, a set of mask images $\mathbf{T}_i$ is generated via thresholding as

$$\mathbf{T}_i(x,y) = \begin{cases} 1 & \text{if } |\mathbf{P}'_i(x,y)| < t \\ 0 & \text{otherwise} \end{cases}, \tag{10}$$

where strong object pixels exceeding a threshold parameter t are set to zero. An example threshold map is shown in Fig. 7. The estimation of the virtual reference scans can be repeated incorporating the mask images. This way pixels which contain a strong object signal are not used for estimating the reference scan, as they might bias the estimate. The refinement step is repeated for a number of k times.

3. EVALUATION

Direct evaluation of the proposed method is challenging. To our knowledge, the effects leading to drifts or changes in the reference phase have not been deeply studied yet. Thus, it is not possible to accurately recreate them in simulation studies. In a first step, we qualitatively analyze the difference between measured reference images and those estimated by our method. Furthermore, we pursue two quantitative approaches for evaluation. Given a simple, homogenous object with a known phase signal, it is possible to compare the output of the proposed method with the classical reference scanning method and the ground truth phase signal of the object. The second approach is to have a group of experts rate the image quality. We compare our method to the classical reference-based scanning approach, with one reference scan per tile-column. The latter approach is our usually used imaging protocol for tiled breast scans, and is a trade-off between reference updates and additional mechanical motion. The data usually show strong drift artifacts, which are sometimes already visible in the first tile acquired after the

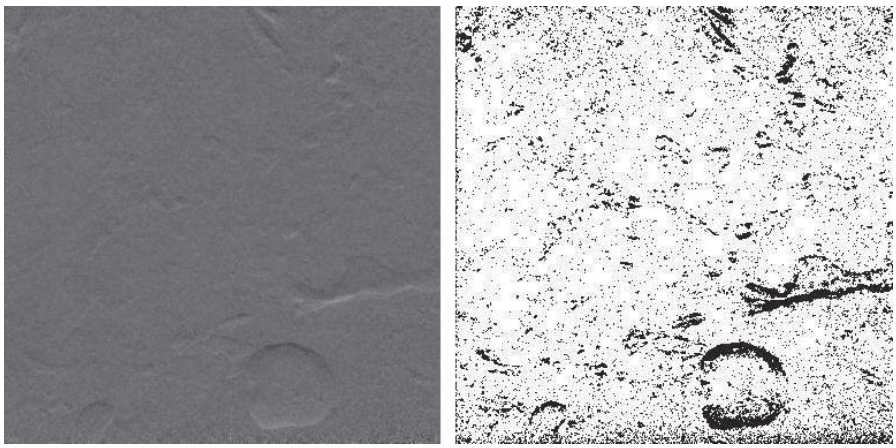

FIG. 7. Computation of the thresholding map $\mathbf{T}_i$. (a) First estimate of the differential phase image $\mathbf{P}'_i$. (b) Corresponding thresholding mask $\mathbf{T}_i$ for $t = 0.1$ after three iterations.

reference scan (for an example see Fig. 9). Thus, we additionally compare our algorithm to the data obtained with classical reference scanning after postprocessing with the shading correction algorithm proposed by Kaeppler et al.[34] This method, to our experience, yields superior results compared to the postprocessing strategy proposed by Tapfer et al.[7] as it additionally uses tile boundary information for the removal of low-frequency drift artifacts.

3.A. Data acquisition and parameter tuning

We performed our evaluation on a set of 21 tiling-based acquisitions of cancerous human mastectomy samples.* The data were acquired using a three-grating Talbot-Lau interferometer. The grating size was 24.14 mm × 13.2 mm, the periods were 24.39 μm (G0), 3.37 μm (G1), and 2.4 μm (G2), with a G1-G2 distance of 159 mm. The design energy of the system was 25 keV, while the X-ray tube was operated at a peak voltage of 40 kVp at 60 mA current. Eight-phase steps were acquired for each tile. More details of the setup can be found in Ref 35. The number of tiles per acquisition varied between $N = 12$ and $N = 88$, and the size of each tile was 380 × 380 pixels. The setup was vertically mounted to mimic a clinical mammography device. Due to the lack of vibration dampening and G0 positioning above the X-ray tube, drifts of the reference signal occurred frequently. This resulted in low-frequency and sometimes also in slight Moirè artifacts in the reconstructed raw images. Before the evaluation, algorithm parameters were manually selected out-of-sample using a separate set of two images. For the proposed method, we set the polynomial degree $d = 5$. The weighting vector $\mathbf{w}$ was set to 0 for polynomial degree 0, to 0.001 for polynomial degrees 1 and 2 and to 1 for higher degrees. Furthermore, the weight vector was multiplied by the number of pixels in each frame for normalization. The window size a for estimating the high-frequency reference phase was set to the number of tiles in the image. Finally, the number of refinement steps k was selected as $k = 3$, as subsequent iterations no longer led to visual changes of the output, while the thresholding parameter was set to $t = 0.1$. For the images postprocessed with the shading correction method,[34] we used linear basis functions with the parameter α set to 100.

*The data were acquired within a study that has been approved by the ethics committee of the University Hospital Erlangen in the medical faculty of the Friedrich-Alexander-University Erlangen-Nuremberg. Written informed consent has been obtained from the patients.

3.B. Qualitative evaluation

For data sets comprised of less than 20 tiles, we computed difference images of the measured reference images and the reference images produced by our algorithm. The resulting images were visually inspected. Specifically we were interested whether the proposed method may be prone to "leaking" of object information into the estimated reference images when the number of tiles is low. Furthermore, we inspected areas where low fringe visibility and/or strong attenuation lead to phase wrapping or uniformly distributed phase noise. For the images used in this experiment, these effects could be observed at metal pins used to fix the specimens (an example can be seen in Fig. 9). We examined whether these artifacts have a negative impact on phase unwrapping, which is a required preprocessing step for the proposed method.

3.C. Evaluation using homogenous objects

Each specimen of our test dataset consisted of a human breast mastectomy sample, compressed between two parallel sheets of PMMA. Some parts of each image contained no specimen. One of these regions was manually marked for each dataset based on the raw data images. The size for each windows was at least 1000 pixels to ensure statistical robustness for the analysis. As these regions only correspond to two parallel slabs of PMMA, their differential phase signal should be constant. Ignoring material imperfections, any signal variation in these windows can be

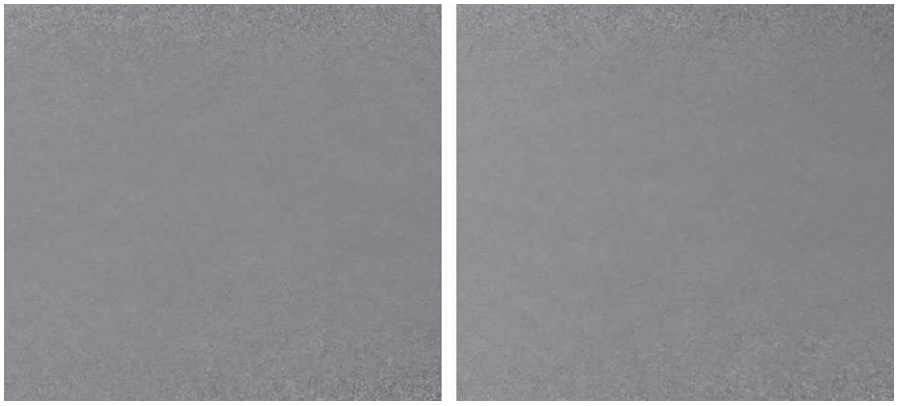

FIG. 8. Difference between measured and virtual reference phase for two tiles of a mastectomy specimen acquisitions with $N = 12$ tiles. Note that no object information can be identified in the difference images.

attributed to either noise or imaging artifacts. For each method and dataset, we calculated the standard deviation of the signals within each window to quantify these signal variations. Note that as our data were generated by a broad-spectrum X-ray source, it is difficult to relate the measured phase variation to a physical phase-shift. Thus, we only calculated the measured phase variations.

3.D. Expert study

Six experts in X-ray imaging provided a manual scoring of the overall image quality for each method and dataset. Each expert was asked to assigned a ranked score from 1 to 5 to each image, whereas 5 indicates perfect image quality in absence of artifacts, and 1 indicates poor image quality. The experts were instructed to disregard any image degradations that were not influenced by the reference information (e.g., object-induced phase wraps and tile registration errors).

4. RESULTS

4.A. Qualitative evaluation

Visual inspection of the difference between the measured and the computed reference images revealed low-frequency intensity variations, slight Moirè patterns, and noise. Figure 8 shows two representative tiles from an image comprised of 12 tiles. No signs of "leaked" object signals could be found on any of the difference images.

Local phase wrapping and uniformly distributed phase noise did not impede phase unwrapping step. It remained strictly localized and did not propagate into other image areas (for an example, see Fig. 9).

4.B. Results of homogeneity evaluation and expert study

Results for the homogeneity evaluation and the expert scoring, averaged over all datasets, are given by Table I, while detailed results are listed in Appendix B.

For the homogeneity evaluation, we report for each method the standard deviation in the marked region, averaged over all images and for the worst image. The postprocessing approach yielded more homogenous signals than the raw data in all but two images, while the proposed method yielded the most homogenous signals for all datasets.

For the expert scoring, we report the mean expert score averaged over all images with standard deviation, as well as the mean score for the worst image. The proposed method received the highest score of all methods for all but 2 of the 21 datasets.

5. DISCUSSION

Qualitative analysis of the difference images of the measured and computationally generated reference images revealed no signs of "leaked" object signals in the computed reference images, indicating that the method cleanly separates object and reference information. As the dataset with the smallest number of tiles contained 12 tiles, we conclude that 12 is an upper bound of the number of tiles required by our method. Future experiments with datasets containing even fewer tiles could reveal more insights on this bound. The low-frequency signals and slight Moirè patterns found in the difference images can be explained by interferometer detuning, which our method is designed to compensate. Unlike in our previous work,[30] we did not observe any ringing artifacts at strong object edges. We attribute this to the fact that the proposed method jointly estimates the references from all tiles. Our qualitative analysis further revealed that the computed reference images contained slightly less noise than the measured reference. This can be attributed to the fact that the measured reference images in our study were acquired with a limited number of phase steps and dose, and that any noise in the reference gets transferred to the phase image upon subtracting the reference from the object image. As the proposed virtual reference is statistically estimated from multiple images, it shows less noise. Thus, the proposed method

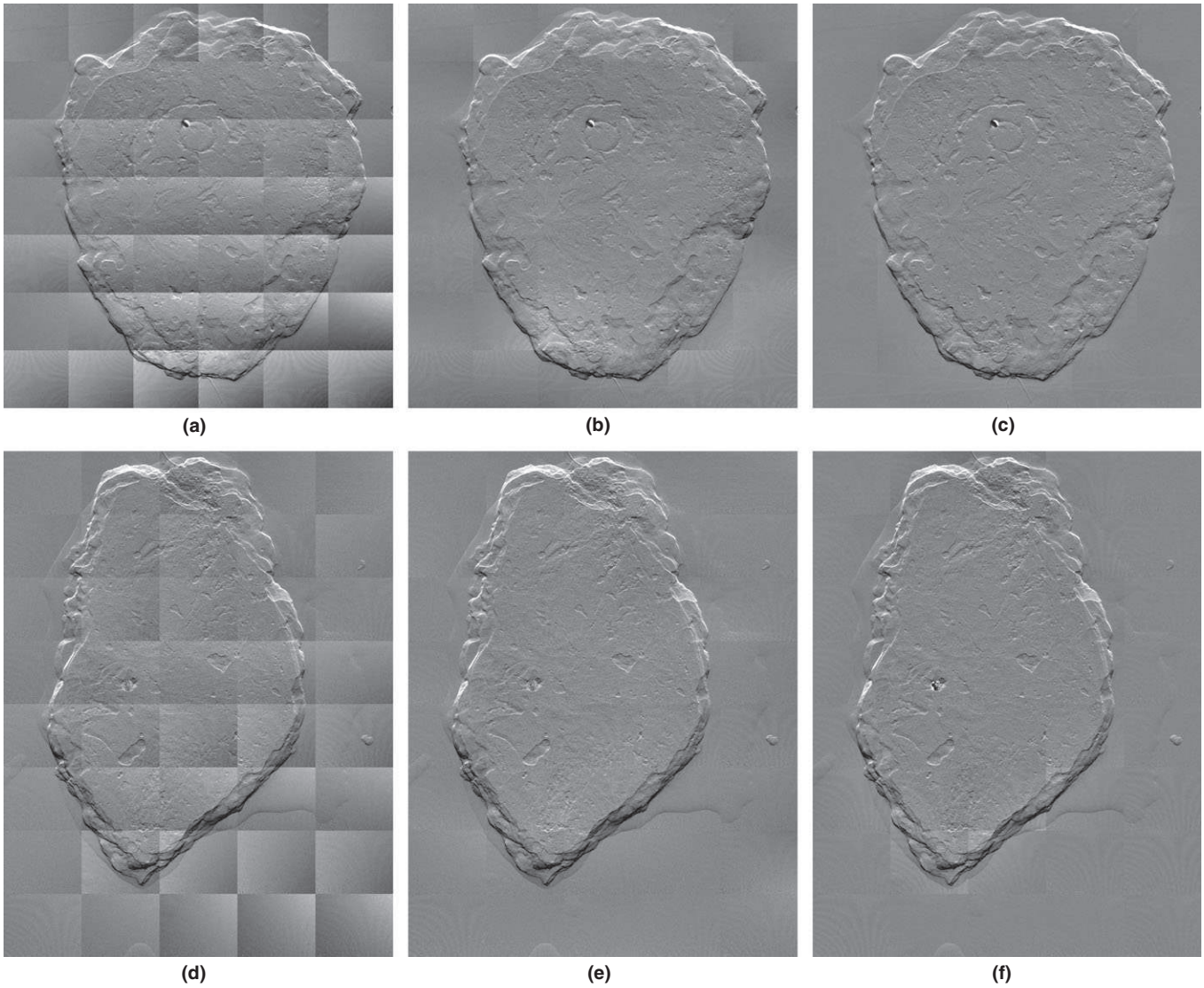

FIG. 9. Two of the images of mastectomy samples used for evaluation. (a,d) Raw data. (b,e) Postprocessed raw data. (c,f) Proposed method. Note that in the raw data images, artifacts due to drift of the reference phase increase from the top tiles towards the bottom tiles. The sample in the bottom row is one of the two samples where the output of the postprocessing method was rated higher than that of the proposed method. We attribute this to the presence of Moirè artifacts in this sample image.

TABLE I. Results of the homogeneity evaluation and expert scoring. Best results are shown in bold. The proposed method yields the lowest inhomogeneity and the highest average expert score.

	Raw data	Postprocessed	Proposed method
Homogeneity Evaluation			
Average std. dev.	0.06 ± 0.03	0.04 ± 0.02	0.03 ± 0.01
Std. dev. of worst dataset	0.1	0.08	0.05
Expert Scoring			
Average of mean score	1.6 ± 0.4	3.0 ± 0.4	4.04 ± 0.5
Mean score of worst dataset	1.0	2.2	2.2

may be advantageous in terms of noise if time constraints prohibit the acquisition of a noise-free reference image.

For all datasets, the proposed method yielded the lowest standard deviations in the homogenous regions outside of the samples. Most of the signal variation in the images reconstructed from measured reference images was due to low-frequency reference drift. While the postprocessing method removed a bulk of these drift artifacts, the proposed method was more effective in suppressing them. We attribute this to our model of the low-frequency reference phase, which increases robustness to object signals by intertile smoothing, while the postprocessing approach mainly relies on tile boundary information to remove drift artifacts.

The experts assigned the highest score to the images from the proposed method, except for two cases, where they assigned the highest score to the postprocessed images. In these images, most of the tiles showed Moirè artifacts for all three investigated methods. We hypothesize that the presence of the Moirè artifacts negatively influenced the proposed estimation algorithm. Moirè artifacts in Talbot-Lau interferometry haven recently been investigated by Pelzer et al.,[36] who

identified errors during the phase stepping procedure as their underlying cause and proposed an algorithmic solution for suppressing them already during phase reconstruction from the phase stepping data. However, this method was not part of our study.

One limitation of our experiments is that the interferometer used to acquire the data was vertically mounted in order to imitate a clinical mammography system. For vibration-controlled laboratory interferometers, the benefit of the proposed method may be less strong. Another caveat is that our method relies on phase unwrapping as a preprocessing step. While our evaluation showed that our method is robust to local measurement defects due to phase wrapping and noise, we did not investigate the impact of large-area phase wrapping. While we cannot exclude that large-area phase-wraps may become an issue in very general imaging scenarios, we assume that large-area phase-wraps can potentially be avoided when scanning relatively homogeneous materials such as breasts by selecting an appropriate design energy and setup sensitivity.

6. CONCLUSIONS AND OUTLOOK

Talbot-Lau X-ray imaging is an emerging imaging technique. Despite initial encouraging results, several problems still need to be addressed for translation of this technique to clinical use. In this paper, we presented a computational method for obtaining the reference phase for a tiled grating-based X-ray phase-contrast system instead of measuring it. We expect that the proposed algorithm improves the practical applicability of tiling-based phase-contrast imaging due to simplification of the acquisition process. Furthermore, our experiments show that the method improves the quality of the resulting images. While absorption and dark-field signals typically suffer from much less drift artifacts, extending the algorithm to these images could be worthwhile. In principle, the proposed method could also be used for reference-free Talbot-Lau phase-contrast tomography. However, a tomographic acquisition is likely to violate the assumption that the content of subsequent tiles is uncorrelated. We will investigate this possibility in future work.

ACKNOWLEDGMENTS

Sebastian Kaeppler gratefully acknowledges funding from the International Max Planck Research School - Physics of Light (IMPRS-PL). This work was partially supported by the Research Training Group 1773 *Heterogeneous Image Systems*, funded by the German Research Foundation (DFG).

CONFLICT OF INTEREST

The authors have no conflicts of interest to disclose.

APPENDIX A: OPTIMIZATION SCHEME FOR ESTIMATING THE LOW-FREQUENCY PHASE IMAGES

The optimization problem in Eq. 5 for obtaining the set of polynomial coefficient $\mathbf{P}$ is:

$$\arg\min_{\mathbf{P}} \sum_{i=1}^{N} \|\mathbf{M}\cdot\mathbf{p}_i - \mathbf{O}_i^{\mathrm{u}}\|_1 + \sum_{i=1}^{N-1}\frac{1}{2}\|\mathbf{p}_i - \mathbf{p}_{i+1}\|_{\mathbf{w}}^2. \quad (11)$$

It is difficult to solve this problem directly due to (a) problem size and (b) the combined use of the L1- and weighted L2-norm. Typically, L1-norm regression problems are solved directly by linear programming,[37] or iteratively using the Alternating Direction Method of Multipliers (ADMM,[32]) or Iteratively Reweighted Least Squares.[38] However, these methods are designed to handle pure L1-norm problems without an additional weighted L2 term. Furthermore, iterative approaches require the inversion of a matrix that considers the pixels of all tiles and all polynomial coefficients simultaneously. Due to this fact, the number of matrix entries grows quadratically with the number of tiles. The inversion of such a matrix is usually intractable for our problem size (as an example, assuming 300 × 300 pixels per tile, 40 tiles, polynomial degree 5, the corresponding matrix would have approximately 130 million entries). We propose an extended ADMM-type optimization scheme, exploiting the loose coupling between the polynomial coefficients of distant tiles, thereby solving the optimization problem efficiently. We introduce a set of splitting variables $\mathbf{Z} = [\mathbf{z}_1, \mathbf{z}_2, \ldots \mathbf{z}_N]$ and rewrite Eq. 11 in a constrained form:

$$\begin{aligned} &\arg\min_{\mathbf{P},\mathbf{Z}} \sum_{i=1}^{N} \|\mathbf{z}_i\|_1 + \sum_{i=1}^{N-1}\frac{1}{2}\|\mathbf{p}_i - \mathbf{p}_{i+1}\|_{\mathbf{w}}^2 \\ &\text{subject to} \quad \mathbf{z}_i = \mathbf{M}\cdot\mathbf{p}_i - \mathbf{O}_i^{\mathrm{u}} \quad \forall i. \end{aligned} \quad (12)$$

Note that for any feasible (i.e., constraint-fulfilling) choice of $\mathbf{P}$ and $\mathbf{Z}$, this problem is equivalent to the original optimization problem. The corresponding *augmented* Lagrangian of this problem is

$$\begin{aligned} \hat{L}(\mathbf{P},\mathbf{Z},\lambda) = &\sum_{i=1}^{N} \|\mathbf{z}_i\|_1 + \sum_{i=1}^{N-1}\frac{1}{2}\|\mathbf{p}_i - \mathbf{p}_{i+1}\|_{\mathbf{w}}^2 \\ &+ \sum_{i=1}^{N} \lambda_i(\mathbf{z}_i - (\mathbf{M}\cdot\mathbf{p}_i - \mathbf{O}_i^{\mathrm{u}})) \\ &+ \sum_{i=1}^{N}\frac{\rho}{2}\|\mathbf{z_i} - (\mathbf{M}\cdot\mathbf{p}_i - \mathbf{O}_i^{\mathrm{u}})\|_2^2 \end{aligned} \quad (13)$$

Here, $\lambda = [\lambda_1, \lambda_2, \ldots, \lambda_N]$ is the matrix of the Lagrangian multipliers, and $\rho > 0$ is a scalar penalty parameter. Note that for any feasible choice of $\mathbf{P}$ and $\mathbf{Z}$, the penalty term vanishes. The augmented Lagrangian can be rearranged[32] as:

$$\hat{L}(\mathbf{P},\mathbf{Z},\lambda) = \sum_{i=1}^{N} \|\mathbf{z}_i\|_1 + \sum_{i=1}^{N-1} \frac{1}{2} \|\mathbf{p}_i - \mathbf{p}_{i+1}\|_{\mathbf{w}}^2 + \sum_{i=1}^{N} \frac{\rho}{2} (\|(\mathbf{z}_i - (\mathbf{M}\cdot\mathbf{p}_i - \mathbf{O}_i^{\mathrm{u}})) + (1/\rho)\lambda_i\|_2^2 - \|(1/\rho)\lambda_i\|_2^2) \tag{14}$$

The ADMM method minimizes the constrained objective function by iteratively minimizing $\hat{L}(\mathbf{P},\mathbf{Z},\lambda)$ with respect to the primal variables, followed by an gradient ascent update of the dual variables. However, the update of primal variables is performed *alternatingly*, i.e., one variable is updated after another. Using j as an iteration counter, the update rules are:

$$\mathbf{P}^{j+1} = \arg\min_{\mathbf{P}} \hat{L}(\mathbf{P},\mathbf{Z}^j,\lambda^j) \tag{15}$$

$$\mathbf{Z}^{j+1} = \arg\min_{\mathbf{Z}} \hat{L}(\mathbf{P}^{j+1},\mathbf{Z},\lambda^j) \tag{16}$$

$$\lambda_i^{j+1} = \lambda_i^j + \rho(\mathbf{z_i}^{j+1} - (\mathbf{M}\cdot\mathbf{p}_i^{j+1} - \mathbf{O}_i^{\mathrm{u}})) \tag{17}$$

The update of the dual variables λ can be computed directly from the constraint violation. The joint update of $\mathbf{Z}$ decouples to the element-wise L1 proximal operator, i.e., soft-thresholding:

$$\mathbf{z}_i^{j+1} = \mathrm{prox}_{\frac{\rho}{2}\|\cdot\|_1}[(\mathbf{z_i} - (\mathbf{M}\cdot\mathbf{p}_i^{j+1} - \mathbf{O}_i^{\mathrm{u}})) + (1/\rho)\lambda_i^j] \tag{18}$$

$$\mathbf{z}_i^{j+1} = \arg\min_{\mathbf{z}_i} \|\mathbf{z}_i\|_1 + \frac{\rho}{2}(\|(\mathbf{z_i} - (\mathbf{M}\cdot\mathbf{p}_i^{j+1} - \mathbf{O}_i^{\mathrm{u}})) + (1/\rho)\lambda_i^j\|_2^2 \tag{19}$$

The update rule for the polynomial coefficients $\mathbf{P}$ is:

$$\mathbf{P}^{j+1} = \arg\min_{\mathbf{P}} \hat{L}(\mathbf{P},\mathbf{Z}^j,\lambda^j) \tag{20}$$

$$\mathbf{P}^{j+1} = \arg\min_{\mathbf{P}} \sum_{i=1}^{N-1} \frac{1}{2} \|\mathbf{p}_i - \mathbf{p}_{i+1}\|_{\mathbf{w}}^2 + \sum_{i=1}^{N} \frac{\rho}{2}(\|(\mathbf{z}_i^j - (\mathbf{M}\cdot\mathbf{p}_i - \mathbf{O}_i^{\mathrm{u}}) + (1/\rho)\lambda_i^j\|_2^2) \tag{21}$$

This problem can be reformulated as weighted least squares problem. Still, as indicated above, the resulting matrix inversion is intractable due to the matrix size. However, we note that the variables from one tile are only coupled to those of the neighboring tiles by their corresponding smoothness terms. Thus, the combined matrix shows a strong block structure that can be exploited. Here, we do not solve for $\mathbf{P}$ directly. Instead, we update its components iteratively:

$$\mathbf{p}_i^{j+1} = \arg\min_{\mathbf{p}_i} \hat{L}(\mathbf{p}_1^{j+1},\ldots,\mathbf{p}_i,\mathbf{p}_{i+1}^j,\ldots,\mathbf{p}_N^j,\mathbf{Z}^j,\lambda^j) \tag{22}$$

$$\mathbf{p}_i^{j+1} = \arg\min_{\mathbf{p}_i} \frac{1}{2}\|\mathbf{p}_i - \mathbf{p}_{i-1}^{j+1}\|_{\mathbf{w}}^2 + \frac{1}{2}\|\mathbf{p}_i - \mathbf{p}_{i+1}^j\|_{\mathbf{w}}^2 + \frac{\rho}{2}(\|(\mathbf{z}_i^j - (\mathbf{M}\cdot\mathbf{p}_i - \mathbf{O}_i^{\mathrm{u}}) + (1/\rho)\lambda_i^j\|_2^2) \ (1<i<N) \tag{23}$$

This problems corresponds to a least squares problem with generalized Tikhonov regularization and only requires the inversion of $\mathbf{M}^T\rho\mathbf{IM} + 2(\mathbf{w}^T\mathbf{I})$. This matrix inversion is tractable, because the number of matrix entries is only the number of pixels times the number of polynomial coefficients. We also note that the inverse, when computed once, can be stored for further iterations. The proposed iteration scheme is in some sense similar to the Gauss–Seidel method, except that whole matrix blocks are used to update the solution, instead of single matrix rows. We note that this step no longer leads to a minimization of $\hat{L}(\mathbf{P},\mathbf{Z},\lambda)$ with respect to the polynomial coefficients $\mathbf{P}$. Instead, the value of the augmented Lagrangian is only decreased. However, convergence of the ADMM algorithm is still achieved in this case.[32]

Convergence speed of the ADMM method is highly dependent on the choice of the penalty parameter ρ. In pilot experiments, we found $\rho = 1.0$ to be a good choice for a wide range of weight vectors $\mathbf{w}$, while a number of 100 iterations seemed to be sufficient to achieve a stable solution. The optimizing scheme required a runtime of 34 s for a sample dataset (36 tiles, 300 × 300 pixels per tile, polynomial degree 5) running on a standard laptop (DELL M4800, Intel Core i7-4910MQ CPU, 32 GB RAM, MATLAB 2014b).

APPENDIX B: DETAILED RESULTS OF THE EVALUATION

TABLE A1. Detailed results of the homogeneity evaluation and expert scoring. The best result for each dataset is shown in bold.

	Homogeneity - Std. Dev.			Reader study - mean score		
Dataset	Raw data	Postprocessed	Proposed	Raw data	Postprocessed	Proposed
1	0.05	0.03	**0.02**	1.5	3.0	**4.0**
2	0.08	0.03	**0.02**	1.2	2.3	**4.2**
3	0.04	0.02	**0.01**	2.5	3.1	**4.3**
4	0.03	**0.02**	**0.02**	1.7	3.0	**4.2**
5	0.07	0.03	**0.02**	1.2	2.7	**4.2**
6	0.05	0.04	**0.02**	1.8	3.3	**4.3**
7	0.02	**0.02**	**0.02**	1.33	3.3	**4.2**
8	0.02	0.02	**0.01**	1.8	3.2	**4.3**
9	0.06	0.03	**0.02**	1.3	3.2	**4.5**
10	0.03	0.03	**0.02**	1.8	3.3	**4.5**
11	0.02	**0.02**	**0.02**	1.8	3.5	**4.2**
12	0.05	0.03	**0.02**	1.3	3.2	**4.2**
13	0.03	**0.02**	**0.02**	2.2	3.3	**4.2**
14	0.09	0.08	**0.05**	1.3	**3.2**	2.2
15	0.09	0.08	**0.05**	1.2	2.3	**3.7**
16	0.10	0.06	**0.04**	1.3	**3.7**	3.0
17	0.06	0.05	**0.04**	1.5	2.8	**3.8**
18	0.05	0.05	**0.04**	1.2	2.8	**4.0**
19	0.06	0.06	**0.04**	1.7	3.2	**4.0**
20	0.12	0.08	**0.04**	1.0	2.2	**3.7**
21	0.07	0.06	**0.04**	1.3	2.8	**4.0**
avg.	0.06 ± 0.03	0.04 ± 0.02	$\mathbf{0.03 \pm 0.01}$	1.6 ± 0.4	3.0 ± 0.4	$\mathbf{4.0 \pm 0.5}$

[a]Author to whom correspondence should be addressed. Electronic mail: sebastian.kaeppler@fau.de.

REFERENCES

1. Bonse U, Hart M. An xray interferometer with long separated interfering beam paths. *Appl Phys Lett*. 1965;7:99–100.
2. Momose A, Koyama I, Hamaishi Y, Takai K, Suzuki Y, Demonstration of x-ray talbot interferometry. *Jpn J Appl Phys*. 2003;42:L866–L868.
3. Weitkamp T, Diaz A, David C, et al. X-ray phase imaging with a grating interferometer. *Opt Express*. 2005;12:6296–6304.
4. Pfeiffer F, Weitkamp T, Bunk O, David C. Phase retrieval and differential phase-contrast imaging with low-brilliance X-ray sources. *Nat Phys*. 2006;2:258–261.
5. Bech M, Jensen T, Feidenhans R, Bunk O, David C, Pfeiffer F. Soft-tissue phase-contrast tomography with an x-ray tube source. *Phys Med Biol*. 2009;54:2747–2753.
6. Donath T, Pfeiffer F, Bunk O, et al. Toward clinical X-ray phase-contrast CT: Demonstration of enhanced soft-tissue contrast in human specimen. *Invest Radiol*. 2010;45:445–452.
7. Tapfer A, Bech M, Velroyen A, et al. Experimental results from a preclinical x-ray phase-contrast ct scanner. *Proc Natl Acad Sci*. 2012;109:15691–15696.
8. Wang Z, Clavijo CA, Roessl E, et al. Image fusion scheme for differential phase contrast mammography. *J Instrum*. 2013;8:C07011.
9. Pfeiffer F, Bech M, Bunk O, et al. Hard-X-ray dark-field imaging using a grating interferometer. *Nat Mater*. 2008;7:134–137.
10. Lynch SK, Pai V, Auxier J, et al. Interpretation of dark-field contrast and particle-size selectivity in grating interferometers. *Appl Opt*. 2011;50:4310–4319.
11. Bech M, Tapfer A, Velroyen A, et al. In-vivo dark-field and phase-contrast x-ray imaging. *Sci Rep*. 2013;3:3209.
12. Bayer FL, Hu S, Maier A, et al. Reconstruction of scalar and vectorial components in X-ray dark-field tomography. *Proc Natl Acad Sci U S A*. 2014;111:12699–12704.
13. Stampanoni M, Wang Z, Thüring T, et al. The first analysis and clinical evaluation of native breast tissue using differential phase-contrast mammography. *Invest Radiol*. 2011;46:801–806.
14. Grandl S, Scherer K, Sztrókay-Gaul A, et al. Improved visualization of breast cancer features in multifocal carcinoma using phase-contrast and dark-field mammography: an ex vivo study. *Eur Radiol*. 2015;25:3659–3668.
15. Scherer K, Willer K, Gromann L, et al. Toward clinically compatible phase-contrast mammography. *PLoS One*. 2015;10:e0130776.
16. Gromann L, Bequé D, Scherer K, et al. Low-dose, phase-contrast mammography with high signal-to-noise ratio. *Biomed Opt Express*. 2016;7:381–391.
17. Li K, Ge Y, Garrett J, Bevins N, Zambelli J, Chen G-H. Grating-based phase contrast tomosynthesis imaging: Proof-of-concept experimental studies. *Med Phys*. 2014;41:011903.
18. Sarapata A, Stayman JW, Finkenthal M, Siewerdsen JH, Pfeiffer F, Stutman D, High energy x-ray phase contrast ct using glancing-angle grating interferometers. *Med Phys*. 2014;41:021904-1–021904-9.
19. Rieger J, Meyer P, Pelzer G, et al. Designing the phase grating for talbot-lau phase-contrast imaging systems: A simulation and experiment study. *Opt Express*. 2016;24:13357–13364.
20. Momose A, Yashiro W, Kido K, et al. X-ray phase imaging: From synchrotron to hospital. *Phil Trans R Soc A*. 2014;372:20130023.
21. Ge Y, Zhao W, Garrett J, Li K, Chen G-H. Absorption imaging performance in a future talbot-lau interferometer based breast imaging system. In: Hoeschen C, Kontos D, Flohr TG eds. *SPIE Medical Imaging*

Conference, Orlando, FL, 21 February 2015. Vol. Proc. SPIE 9412. Bellingham, WA: SPIE; 2015:94123X–94123X.
22. Pfeiffer F. Gromann L. Willer K. et al. X-ray dark-field chest radiography: A first feasibility study on phantom samples and in-vivo pigs. In: Baron TL, ed. *Annual meeting of the Radiological Society of North America (RSNA), Chicago, IL, 26 November 2016*. Oak Brook, IL: Radiological Society of North America; 2016.
23. Miao H, Chen L, Bennett EE, et al. Motionless phase stepping in X-ray phase contrast imaging with a compact source. *Proc Natl Acad Sci*. 2013;110:19268–19272.
24. Bevins N, Zambelli J, Li K, Qi Z, Chen G.-H. Multicontrast x-ray computed tomography imaging using talbot-lau interferometry without phase stepping. *Med Phys*. 2012;39:424–428.
25. Koehler T, Daerr H, Martens G, et al. Slit-scanning differential x-ray phase-contrast mammography: Proof-of-concept experimental studies. *Med Phys*. 2015;42:1959–1965.
26. Raupach R, Flohr, TG. Analytical evaluation of the signal and noise propagation in X-ray differential phase-contrast computed tomography. *Phys Med Biol*. 2011;56:2219–2244.
27. Sarapata A, Willner M, Walter M, et al. Quantitative imaging using high-energy x-ray phase-contrast ct with a 70 kvp polychromatic x-ray spectrum. *Opt Express*. 2015;23:523–535.
28. Schröter T, Koch F, Meyer P, et al. Large field-of-view tiled grating structures for x-ray phase-contrast imaging. *Rev Sci Instrum*. 2017;88:015104.
29. Roessl E, Daerr H, Koehler T, Martens G, Van Stevendaal U. Clinical boundary conditions for grating-based differential phase-contrast mammography. *Philos Trans R Soc Lond A*. 2014; 372:20130033.
30. Seifert M, Kaeppler S, Hauke C, et al. Optimisation of image reconstruction for phase-contrast x-ray talbot–lau imaging with regard to mechanical robustness. *Phys Med Biol*. 2016;61:6441.
31. Costantini M. A novel phase unwrapping method based on network programming. *IEEE Trans Geosci Remote Sens*. 1998;36:813–821.
32. Boyd S, Parikh N, Chu E, Peleato B, Eckstein J. Distributed optimization and statistical learning via the alternating direction method of multipliers. *Found Trends Mach Learn*. 2011;3:1–122.
33. Hettmansperger T, McKean J. *Robust Nonparametric Statistical Methods*. Boca Raton, FL: CRC Press; 2010.
34. Käppler S, Wandner J, Weber T, et al. Shading correction for grating-based differential phase contrast X-ray imaging. In: Lavietes A, ed. *IEEE Nuclear Science Symposium and Medical Imaging Conference (NSS/MIC), Seattle, WA, 8 November 2014*. Piscataway, NJ: IEEE; 2014.
35. Michel T, Rieger J, Anton G, et al. On a dark-field signal generated by micrometer-sized calcifications in phase-contrast mammography. *Phys Med Biol*. 2013;58:2713–2732.
36. Pelzer G, Rieger J, Hauke C, et al. Reconstruction method for grating-based x-ray phase-contrast images without knowledge of the grating positions. *J Instrum*. 2015;10:P12017.
37. Boyd S, Vandenberghe L. *Convex Optimization*. Cambridge: Cambridge University Press; 2004.
38. Daubechies I, DeVore R, Fornasier M, Güntürk C, Iteratively reweighted least squares minimization for sparse recovery. *Commun Pure Appl Math*. 2010;63:1–38.